Manuscript Click here to view linked References

Enhanced Photocatalytic Efficiency of Bi_2MoO_6 for Water and *p*-Nitroaniline Reduction via Iodate (I^{5+}) Substitution: Implications of Small Polaron Formation

Anurak Waehayee,[a,b] Lappawat Ngamwongwan,[c] Andreas Kafizas,[d,e] Tammanoon Chankhanittha,[f,g] Teera Butburee,[f] Hideki Nakajima,[h] Suttipong Wannapaiboon,[h] Soraya Pornsuwan,[i] Suwit Suthirakun,[a] Theeranun Siritanon [a*]

[a] School of Chemistry, Institute of Science, Suranaree University of Technology, 111 University Avenue, Muang, Nakhon Ratchasima, 30000, Thailand.

[b] Institute of Research and Development, Suranaree University of Technology, 111 University Avenue, Muang, Nakhon Ratchasima, 30000, Thailand.

[c] School of Physics, Institute of Science, Suranaree University of Technology, 111 University Avenue, Muang, Nakhon Ratchasima, 30000, Thailand.

[d] Department of Chemistry, Molecular Science Research Hub, Imperial College London, White City, London, W12 0BZ, U.K.

[e] London Centre for Nanotechnology, Imperial College London, London, SW7 2AZ, U.K.

[f] National Nanotechnology Center, National Science and Technology Development Agency, 111 Thailand Science Park, Pathum Thani 12120, Thailand.

[g] Materials Chemistry Research Center (MCRC), Department of Chemistry, Faculty of Science, Khon Kaen University, Khon Kaen 40002, Thailand.

[h] Synchrotron Light Research Institute, 111 University Avenue, Nakhon Ratchasima 30000, Thailand.

[i] Department of Chemistry, Faculty of Science and Center of Excellence for Innovation in Chemistry, Mahidol University, Bangkok 10400, Thailand.

*Corresponding author e-mail: theeranun@sut.ac.th

Abstract

The wide range of potential applications for photocatalysis has made research on photocatalytic materials highly active. However, various limitations hinder large-scale applications of photocatalysis, making the search for novel and improved catalysts an ongoing pursuit. To achieve this, a detailed analysis of material characteristics and charge transfer behavior is crucial. This study investigates the enhancement of Bi_2MoO_6 (BMO) photocatalytic performance through iodate (I^{5+}) substitution, focusing on its impact on charge transport and reaction efficiency. Employing experimental and computational methods, we demonstrate for the first time that carrier migration in Bi_2MoO_6 follow a small polaron model. Substituting I^{5+} into Bi_2MoO_6 increase the exposure on {100} facets, where polaron hopping along the facet is easier than on the exposed {010} facet of pristine Bi_2MoO_6. Moreover, this substitution creates defects and increases charge carrier concentration by approximately threefold. The increased Fermi energy level enables I-doped Bi_2MoO_6 to generate H_2 and enhance p-nitroaniline reduction activity. As a result, the catalyst exhibits nearly 10 times higher efficiency in both reactions. This approach utilizes defect engineering and polaronic transport to improve photocatalyst design, presenting a promising solution for sustainable energy applications, including water splitting and selective organic transformations.

Graphical abstract

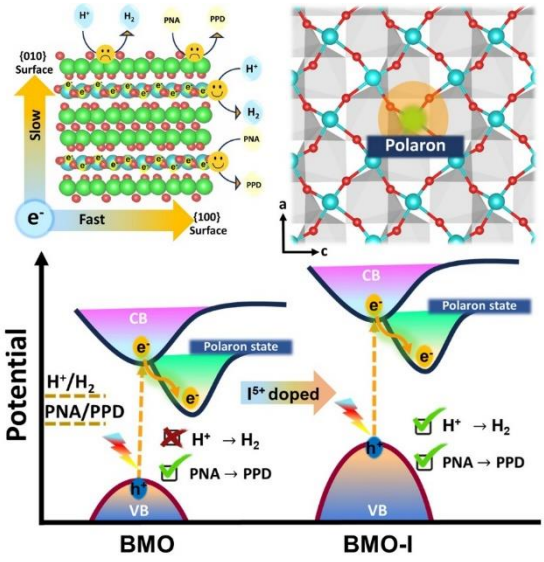

Keywords: Polaron, Bi_2MoO_6, Photocatalyst, H_2 production, *p*-Nitroaniline reduction

1. Introduction

Since most solar energy falls within the visible spectrum, researchers have been working to develop and modify visible-light-driven materials to tackle energy shortages and environmental challenges. Transition metal oxides (TMOs) with visible-light photocatalytic properties are of particular interest [1]. Photocatalysis has been widely used in various applications, such as hydrogen and oxygen production through water splitting, CO_2 reduction into valuable compounds, organic synthesis under mild conditions, and the degradation of organic pollutants [2-4]. Many transition metal oxides (TMOs), such as TiO_2, MoO_3, ZnO, $BiVO_4$, and some perovskites, have been extensively investigated as photocatalysts for solar energy conversion [5-7].

Among these materials, Bi_2MoO_6 has gained significant attention due to its ability to harness visible light for photocatalytic reactions. As a member of the Aurivillius family (n = 1), it features a layered structure comprising perovskite-like $[MoO_4]^{2-}$ layers sandwiched between $[Bi_2O_2]^{2+}$ layers along the b-axis forming a three-dimensional framework with common facet exposures on the (010), (001), and (100) planes[8]. The [010] orientation consists of densely packed $[Bi_2O_2]^{2+}$ layers and $[MoO_4]^{2-}$ octahedra, while the [001] and [100] orientations expose open-channel structures with under-coordinated O, Bi, and Mo atoms. Recent studies have shown that facet exposure significantly affects photocatalytic activity, with certain facets promoting selective redox reactions[9-11]. Electronic structure analysis reveals that the valence band maximum (VBM) arises from the interaction between Bi-6*s* and O-2*p* orbitals, leading to an upward VBM shift that narrows the band gap and enhances light absorption [12]. The conduction band maximum (CBM) is predominantly contributed by Mo-4*d* orbitals, suggesting that photoexcited electron behavior is closely related to Mo. Additionally, the planar average potential profile indicates that the photo-excited electrons tend to localize within the Mo-O layers due to their lower potential, while holes are more likely found near Bi-O[13]. In MoO_6 octahedra, the overlap between Mo $4d^0$ and O 2*p* orbitals results in an uneven charge distribution among oxygen atoms. The long-range ordering of metal cations induces MoO_6 octahedral distortion, commonly referred to as the second-order Jahn-Teller distortion (SOJT-D)[14, 15], which has been shown to enhance charge separation in other oxide photocatalysts[16-18].

Despite its promising properties, Bi_2MoO_6 suffers from low charge transport efficiency and rapid charge recombination, limiting its quantum yield[19]. While doping with various elements and introducing oxygen vacancies have improved charge separation and transport, these strategies have primarily been applied to pollutant degradation, CO_2 reduction, nitrobenzene reduction, and N_2 fixation[20-25]. Notably, there are no reports on enhancing hydrogen production via water splitting using these approaches. Although Bi_2MoO_6 can generate hydrogen under light irradiation, its hydrogen evolution efficiency remains limited by several factors[26, 27]. Additionally, charge transport behavior in Bi_2MoO_6 has not been extensively studied.

This study provides the first evidence of polaron formation in Bi_2MoO_6 and explores the impact of iodate (I^{5+}) substitution on charge separation and transport. Both experimental and computational results reveal that I-doping induces oxygen vacancies, increases electron polaron concentration, and improves electron transport from the bulk to the active surface by expanding the (001) facet. As a result, I^{5+} substitution in Bi_2MoO_6 significantly enhances photocatalytic H_2 production and *p*-nitroaniline reduction efficiency.

2. Results and discussions

2.1 Characterizations

Bi_2MoO_6 (BMO) and I-doped Bi_2MoO_6 (BMO-I) were prepared by a hydrothermal method utilizing CTAB as a surfactant (More details on the preparation and characterizations are provided in the Supplementary Information). The crystal structures of the samples were analyzed using X-ray diffraction (XRD) patterns, as shown in Fig. 1a. All diffraction peaks correspond to the orthorhombic structure of γ-Bi_2MoO_6 (JCPDS No. 21-0102)[28], with no impurity peaks detected. A magnified view of the XRD patterns in the 27–34° range (Fig. 1b) reveals the diffraction peaks corresponding to the (131), (200), and (060) crystal planes. Notably, the peaks shift to lower 2θ values with increasing iodine content, indicating an expansion of the crystal lattice due to iodine incorporation. The expansion can be attributed to the larger ionic radius of iodine (I^{5+}, 0.95 Å) compared to molybdenum (Mo^{6+}, 0.59 Å)[29]. The crystal lattice parameters of BMO with varying iodine content are summarized in Table 1, showing a more pronounced increase in the b- parameter relative to the a and c parameter as iodine content rises (Fig. 1c). Additionally, the intensity ratio of the (060)/(200) peaks changes significantly with increasing iodine doping. This variation reflects the influence of I^{5+} ions on the preferential growth orientation of BMO crystals.

To gain deeper insight into the influence of iodine (I) doping on the local structure of Bi_2MoO_6, the samples were analyzed by Raman spectroscopy[30]. The Raman bands in the 600–900 cm^{-1} range are typically associated with Mo–O stretching modes in distorted MoO_6 octahedra. Specifically, the band at 717 cm^{-1} corresponds to the asymmetric stretching vibrations of equatorial oxygen atoms ($Mo–O_{Eq}$) connecting the MoO_6 octahedra within the perovskite-like layers. Meanwhile, the bands at 798 and 830 cm^{-1} are attributed to the symmetric and asymmetric stretching modes of apical oxygen atoms ($Mo–O_{Ap}$), respectively[30]. As shown in Fig. 1d, the splitting between the symmetric and asymmetric stretching modes of apical oxygen atoms increases with higher iodine content, indicating a greater degree of SOJT distortion[31]. The metal-oxygen bond lengths ($R_{Mo–O}$) were calculated using the empirical equation: $R_{Mo–O}$ = 0.48239ln(32895/ν), where ν represents the Raman stretching frequency in wavenumbers[32]. The calculated Mo–O bond lengths, presented in Fig. 1e, show a gradual increase in both apical and equatorial Mo–O distances with increasing iodine doping. The expansion is more pronounced in the apical direction, consistent with the XRD results. Additionally, our calculation indicates that substitution of 6.25% iodine in the lattice increases the MoO_6 octahedral distortion by approximately 3.17% (Fig. 1f; More details provided in the Supplementary Information).

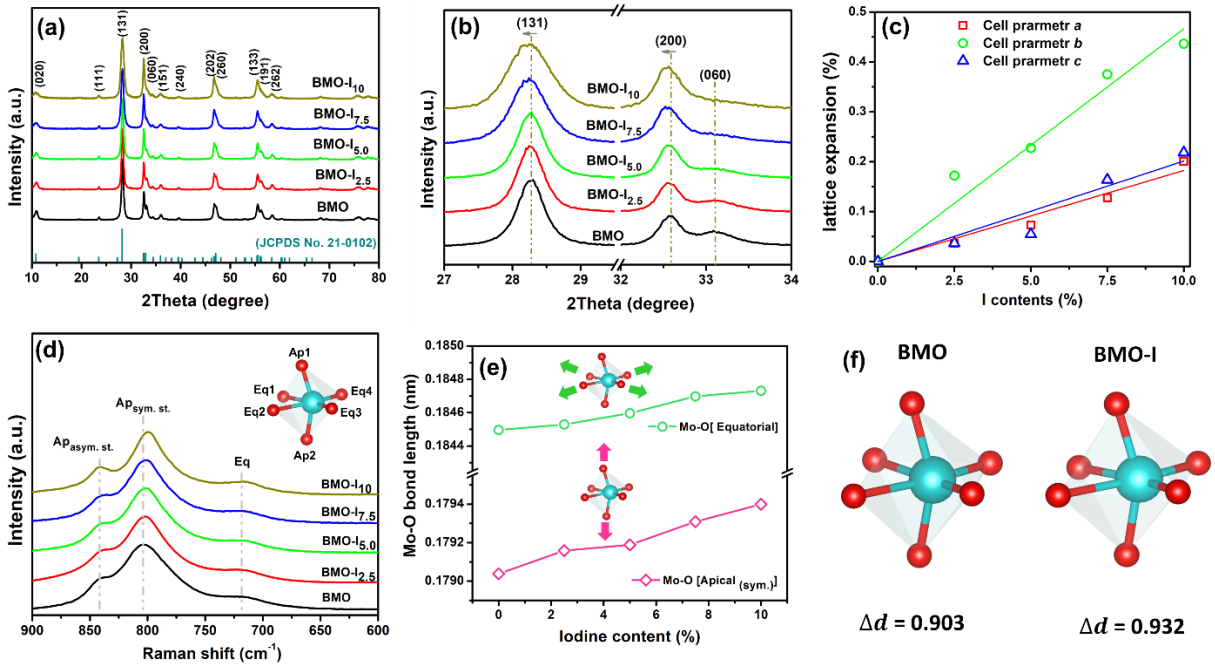

Fig. 1 XRD patterns (a), the enlarged XRD patterns (b), a plot of lattice expansion (c), the enlarged Raman spectra (d), and calculated Mo-O bond lengths (e) of BMO-I_x (x = 0.0, 2.5, 5.0, 7.5 and

10%mol). The local structure of MoO_6 with the magnitude of the SOJT-D (Δd) of BMO and BMO-I (f).

Table 1 Cell Parameters, Cell Volumes (V), and Peak Intensity Ratios of the Samples.

Compound	Cell parameter (Å)			V ($Å^3$)	Peak Intensity Ratios; (I_{060}/I_{200})
	a	*b*	*c*		
BMO	5.480(1)	16.271(4)	5.498(1)	490.3(2)	0.53
BMO-$I_{2.5}$	5.482(2)	16.299(5)	5.500(2)	491.4(3)	0.44
BMO-$I_{5.0}$	5.484(1)	16.308(4)	5.501(1)	492.0(2)	0.35
BMO-$I_{7.5}$	5.487(2)	16.332(6)	5.507(2)	493.5(3)	0.29
BMO-I_{10}	5.491(1)	16.342(4)	5.510(2)	494.4(2)	0.24

The morphology of pristine BMO and BMO-$I_{5.0}$ was investigated using scanning electron microscopy (SEM) and transmission electron microscopy (TEM). Both samples exhibit nanosheet-like structures, as shown in Fig. 2a-d. High-resolution TEM (HRTEM) images provide insights into the lattice spacing (insets in Fig. 2c and d). For pristine BMO, the measured lattice spacings of 0.275 and 0.274 nm correspond to the (002) and (200) planes, respectively, forming a 90° angle. This confirms that the exposed facets of BMO are predominantly (010) (Fig. 2e) [8]. In contrast, the BMO-$I_{5.0}$ sample reveals lattice spacings of 0.274 nm and 0.269 nm, attributed to the (200) and (060) planes, respectively (inset in Fig. 2d). This indicates that BMO-I is primarily exposed with (100) facets (Fig. 2f)[11]. These interplanar spacing values align with the XRD results, supporting the conclusion that iodine doping alters the preferential growth direction of BMO crystals. Using the atomic force microscopy (AFM), the thicknesses of pristine BMO and BMO-$I_{5.0}$ are approximated to 14.4 nm and 4.9 nm, respectively (Fig. 2g and h), confirming the nanosheet morphology, consistent with the SEM and TEM results. The specific surface area of the samples was measured using the Brunauer–Emmett–Teller (BET) method. As shown in Fig. 2i, both BMO and BMO-$I_{5.0}$ exhibit N_2 adsorption and desorption isotherms with hysteresis loops in the P/P_0 range of 0.8–1.0. This behavior is attributed to slit-like mesopores and macropores formed by the

aggregation of nanosheets[33]. The BET surface area of BMO is 20.07 m^2/g, while that of BMO-$I_{5.0}$ is slightly higher at 26.29 m^2/g.

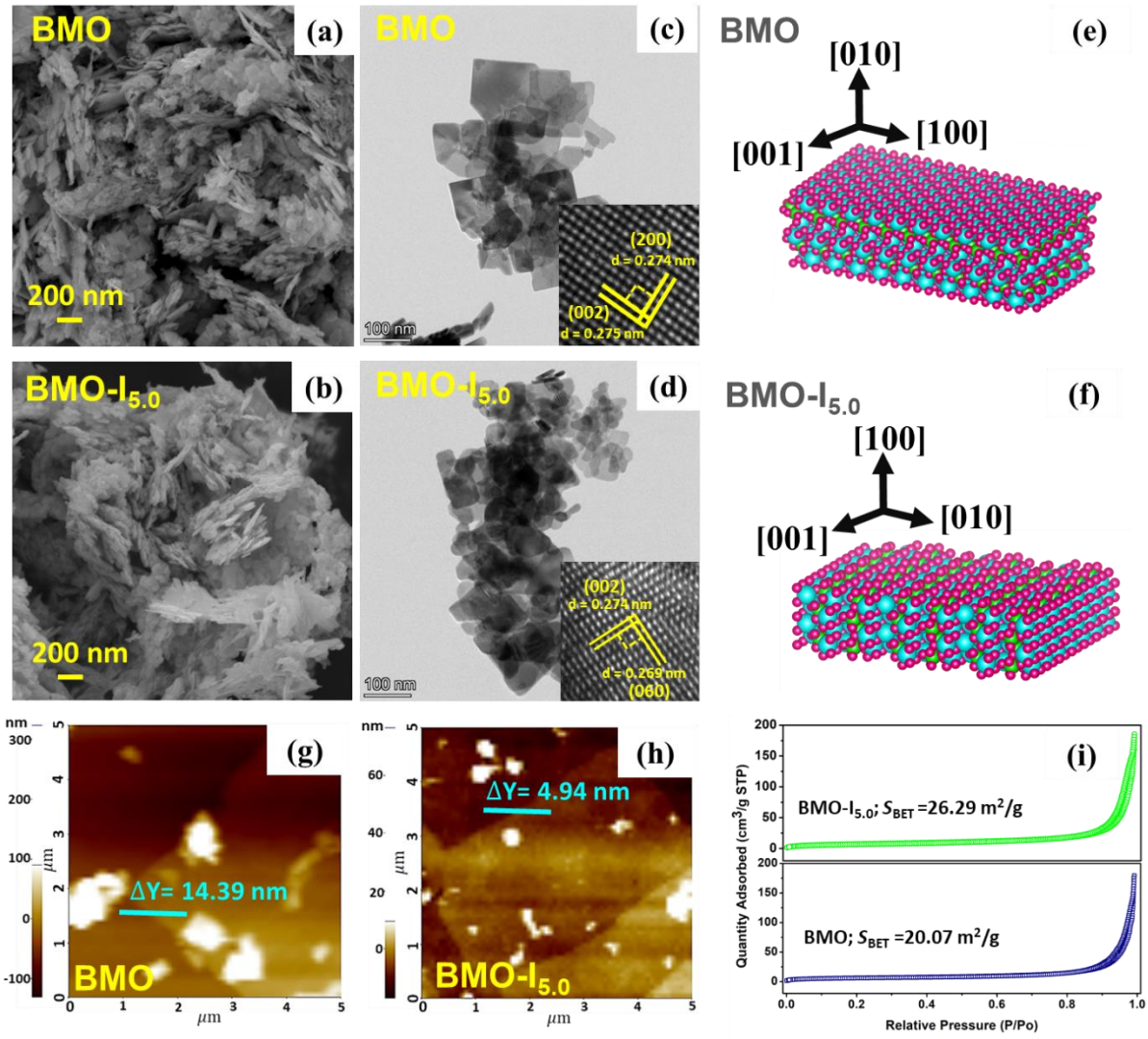

Fig.2 SEM images (a, b), TEM images (c, d), HRTEM (inset of c and d), schematic illustration of the crystal orientation (e,f), AFM image (g, h), and BET surface area analysis (i) of BMO and BMO-$I_{5.0}$.

Energy-dispersive X-ray spectroscopy (EDS) elemental mapping as shown in Fig. 3a and b demonstrate the uniform distribution of Bi, Mo, and O in the BMO sample. In the case of BMO-$I_{5.0,}$ the presence of iodine is clearly observed, confirming its successful incorporation with a homogeneous distribution. The chemical states of BMO and BMO-I nanosheets were further examined using X-ray photoelectron spectroscopy (XPS). High-resolution XPS spectra for the I

3*d*, Mo 3*d*, Bi 4*f*, and O 1*s* core levels are presented in Fig. 3c–f. Notably, the I 3*d* core-level spectrum is only detected in the BMO-$I_{5.0}$ sample, with binding energies of I $3d_{5/2}$ and I $3d_{3/2}$ at approximately 623.68 eV and 635.13 eV, respectively, consistent with the I^{5+} oxidation state[34]. The Mo 3*d* spectrum (Fig. 5d) shows two primary peaks corresponding to Mo $3d_{5/2}$ and Mo $3d_{3/2}$, confirming the Mo^{6+} state. Deconvolution of these peaks reveals minor components at lower binding energies, attributed to the Mo^{5+} state[35], which indicates the presence of defects. The Bi 4*f* spectrum (Fig. 5b) shows peaks at 159.14 eV (Bi $4f_{7/2}$) and 164.46 eV (Bi $4f_{5/2}$), corresponding to Bi^{3+} [33]. For O 1*s* spectrum (Fig. 5d), two distinct peaks are observed: one at 529.9–530.1 eV, corresponding to lattice oxygen (O_L), and another at higher binding energies, corresponding to surface oxygen vacancies (O_V)[35]. The O_V/O_L peak area ratio is significantly higher in BMO-$I_{5.0}$ than in pristine BMO, indicating an increased concentration of oxygen vacancies following iodine substitution. The formation of oxygen vacancies (O_V) is a plausible charge compensation mechanism for the substitution of Mo^{6+} with lower-valence I^{5+}. Additionally, a slight shift to lower binding energies in the XPS spectra of BMO-$I_{5.0}$ compared to pristine BMO is observed. This shift can be attributed to the incorporation of I^{5+} ions into the BMO lattice, which influences the electron cloud density. Since I^{5+} has a lower electronegativity than Mo^{6+}, its substitution increases the electronic polarizability and electron cloud density around Bi, Mo, and O atoms, thereby reducing their binding energies.

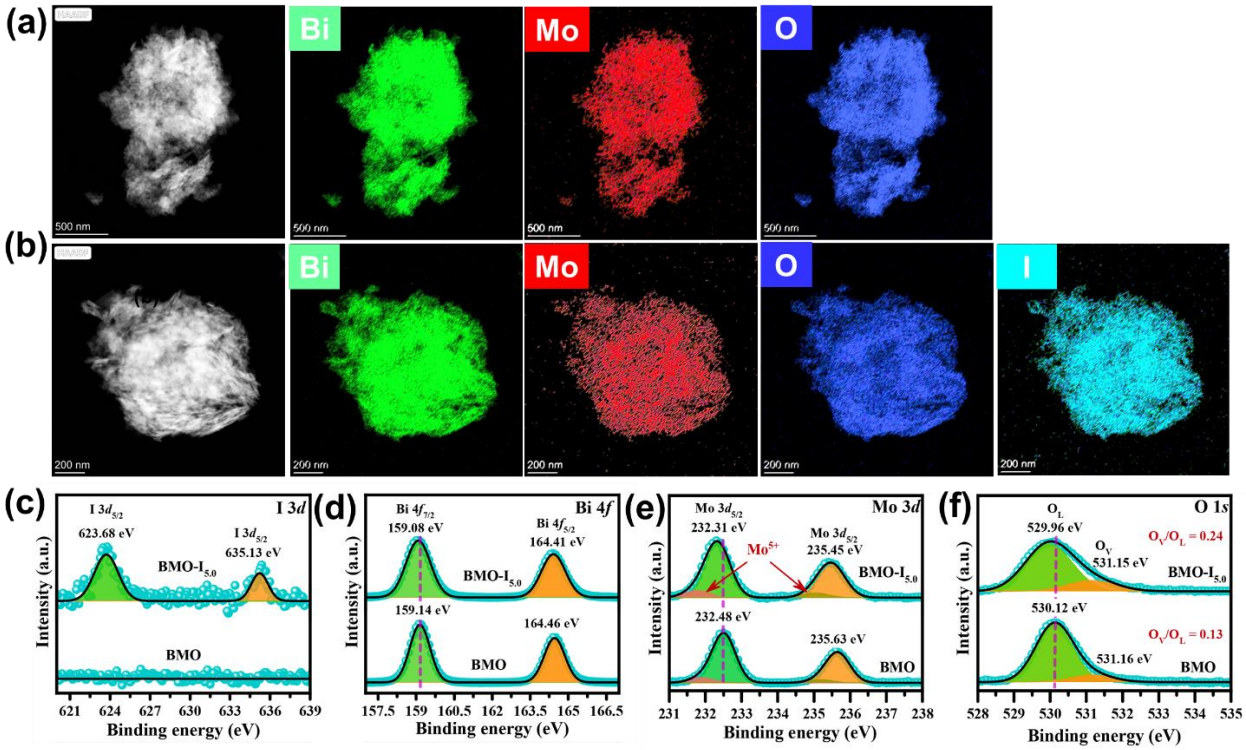

Fig. 3 EDS mapping of BMO (a) and BMO-$I_{5.0}$ (b). I 3d (c), Mo 3d (d), Bi 4f (e), and O 1s (d) XPS spectra of BMO and BMO-$I_{5.0}$

2.2 Photocatalytic properties

The hydrogen evolution reaction (HER) performance of the samples was evaluated using 15% v/v triethanolamine as a hole scavenger and 2wt% Pt as a co-catalyst. As shown in Fig. 4a, all BMO-I samples exhibited HER activity, maintaining a steady H_2 production rate over 3 hours, whereas pristine BMO showed no activity. The H_2 production rate increased with iodine content, reaching a maximum of 77.53 μmol g^{-1} h^{-1} for BMO-$I_{5.0}$. However, BMO-$I_{7.5}$ showed lower activity than BMO-$I_{5.0}$ (inset Fig. 4a). Additionally, the photoreduction of p-nitroaniline (PNA) to *p*-phenylenediamine (PPD) was evaluated for both BMO and BMO-I under nitrogen (N_2) atmosphere using $Na_2C_2O_4$ as a hole scavenger. All BMO-I samples achieved significant conversion rates, outperforming pristine BMO, with BMO-$I_{5.0}$ showing the highest conversion at 9.6 times greater than BMO (Fig. 4b). Bi_2MoO_6 doped with 5.0 mol% iodine demonstrated excellent photocatalytic performance, as well as good reusability. The catalyst maintained a high efficiency of 55.53 μmol g^{-1} h^{-1} in HER and 69.32%conversion p-nitroaniline photooxidation after

three cycles (Fig. 4c). Furthermore, the high stability of the catalyst was confirmed by its unchanged XRD patterns after repeated use (Fig. 4d).

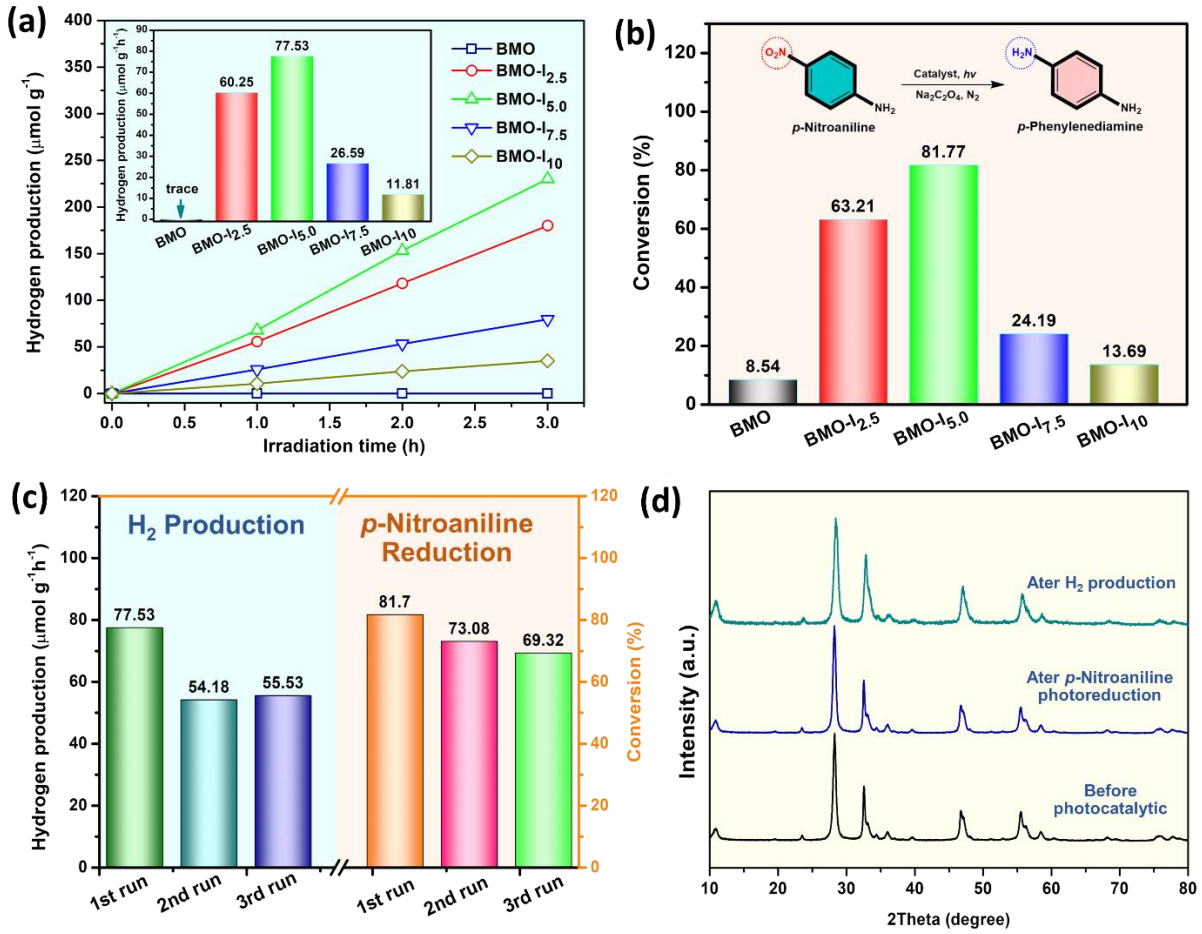

Fig. 4 Photocatalytic H_2 production (a), H_2 generation rate (inset a), and the conversion of p-nitroaniline (b) over pure BMO and BMO-I_x. H_2 generation rate and conversion of p-nitroaniline cycles (c) of BMO-$I_{5.0}$. XRD pattern of the BMO-$I_{5.0}$ before and after the reaction (d).

The UV-Vis absorption spectra of both BMO and I-doped BMO samples with varying iodine (I) contents are presented in Fig. 5a. The band gap energies of all these samples were estimated using the extrapolation of the a Tauc plot of the Kubelka – Munk function (inset Fig. 5a). Interestingly, the introduction of I^{5+} ions does not significantly impact the band gap energies of Bi_2MoO_6. In addition, a combination of UV-Vis (Fig. 5a) and ultraviolet photoelectron spectroscopy (UPS) (Fig. 5b) was used to determine the band edge potentials of the catalysts

(details provided in the Supplementary Information). As shown in Fig. 5c, the conduction band maximum (CBM) and valence band minimum (VBM) potentials of BMO and BMO-$I_{5.0}$ appear suitable for driving both H_2 production (H^+/H_2, -0.41 V vs. RHE at pH 7) and the photocatalytic reduction of PNA to PPD (PNA/PPD, -0.27 V vs. RHE at pH 7). However, previous studies have reported that the position of the electron polaron, which is often located just below the Fermi level (E_F)[36], plays a significant role in water reduction[37]. In this work, we observed that the E_F of BMO-$I_{5.0}$ is approximately -0.52 V, which is more negative compared to H^+/H_2 reduction. In contrast, the E_f of BMO is about -0.33 V, placing it between the reduction levels of H^+ and PNA. This finding suggests that the electrons in BMO may not be as active in the H^+ reduction process but is still active in PNA reduction. Moreover, having E_F close to the H_2O oxidation level increase the likelihood of electron-hole recombination in BMO[38]. The position of E_F in both samples explain how BMO shows no detectable H_2 production but exhibit some PNA reduction ability.

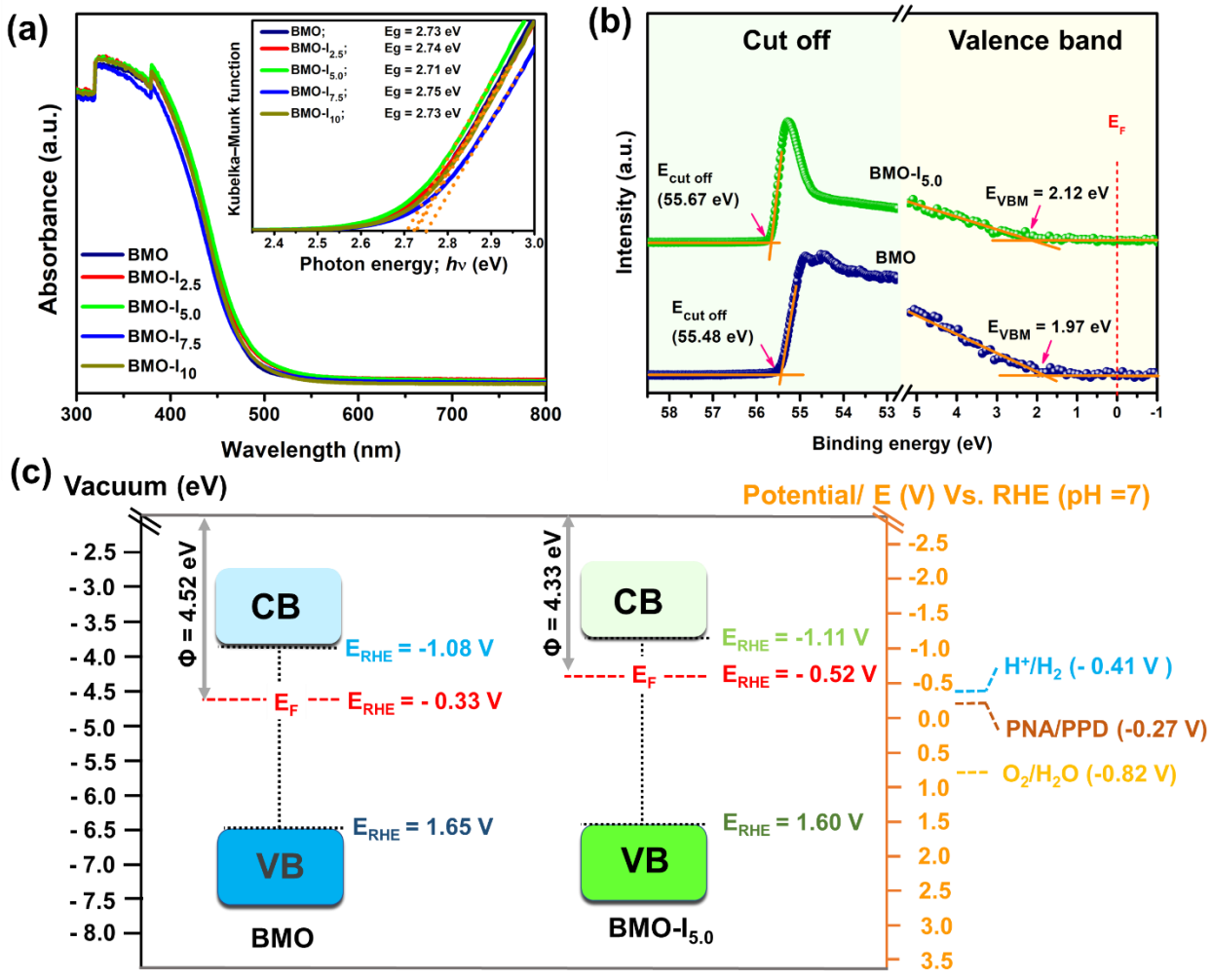

Fig. 5 UV−vis absorption spectra (a) and Kubelka−Munk plot (inset) of BMO and BMO-I_x. UPS spectra (b) and Band energy diagrams (c) of BMO and BMO-$I_{5.0}$.

Charge transport and separation play crucial roles in photocatalytic activity. The efficiency of electron-hole pair separation was examined using the PL technique. As shown in Fig. 6a, the PL intensity of BMO-$I_{5.0}$ is lower than that of BMO when excited at 320 nm, suggesting that I-doping enhances charge separation [31]. The average radiative lifetime (τ_{ave}) was estimated by fitting the time-resolved photoluminescence (TRPL) decay profiles. The results show that BMO-$I_{5.0}$ had a longer carrier lifetime than BMO (Fig. 6b), indicating improved charge separation[39].

Charge carrier behavior was also investigated using transient absorption spectroscopy (TAS) from the 100 μs to 1 s timescale. The transient absorption kinetics for BMO and BMO-$I_{5.0}$ samples are shown in Fig. S1. At the probe wavelength of 600 nm, approximately three times stronger signals were observed in the BMO-$I_{5.0}$ sample (~0.06 %ΔO.D. at 100 μs after the laser pulse) compared to the BMO sample (~0.02 %ΔO.D. at 100 μs after the laser pulse). This indicates that a three-time higher concentration of charge carriers was present in the BMO-$I_{5.0}$ sample compared with the BMO sample (Fig. 6c). Interestingly, the recombination of charge carriers was "log-linear", and could be fit to a logarithmic decay model:

$$\Delta O.D.\ (\%) = -A.\log_{10}(t) + c \qquad \text{(Eq. 1)}$$

where ΔO.D. (%) is the concentration of charge carriers at time, and A and c are fitting constants. Previous work has suggested that such logarithmic decay occurs when tunneling contributes significantly to charge transport [40]. This indicates that at least one type of the charge carriers (either the electrons or holes) in Bi_2MoO_6 is static and thus polaronic in nature. The transient absorption spectra for BMO and BMO-$I_{5.0}$ at select times are shown in Fig. S2. Despite early timescale (100 μs to 1 ms) bleaching phenomena in BMO, which may be attributed to the temporary loss of mid-gap transitions from defect states, broadband photoinduced absorption features were observed from 10 ms onward, with the highest absorption seen in the blue region, attributed to ultra-bandgap electron-hole carrier absorption. Similar features appeared in BMO-$I_{5.0}$, but without early timescale bleaching. The photoinduced absorption at 600 nm was investigated at a range of laser powers, from ~426 to ~38.4 μJ.cm^{-2} per pulse, for BMO and BMO-$I_{5.0}$ (Fig. S3). A plot of the laser power against ΔO.D. (%) at select times (Fig. S4) revealed a near-

linear dependence of charge carrier concentration on laser power. This further supports polaron formation, as systems with more mobile charges typically exhibit sub-linear dependence due to the increased probability of bimolecular recombination at higher charge carrier concentrations.

Photocurrent density measurements under light irradiation (Fig. 6d) revealed a higher current density in BMO-$I_{5.0}$, implying enhanced electron-hole separation and greater charge density due to I-doping. Since photogenerated electron-hole pairs must migrate from the bulk to active surface sites for redox reactions, electrochemical impedance spectroscopy (EIS) was conducted to assess charge-transfer resistance. The Nyquist plots in Fig. 6e show that BMO-$I_{5.0}$ exhibited a significantly smaller impedance arc radius than BMO, indicating a lower charge-transfer resistance and superior carrier transport ability[39].

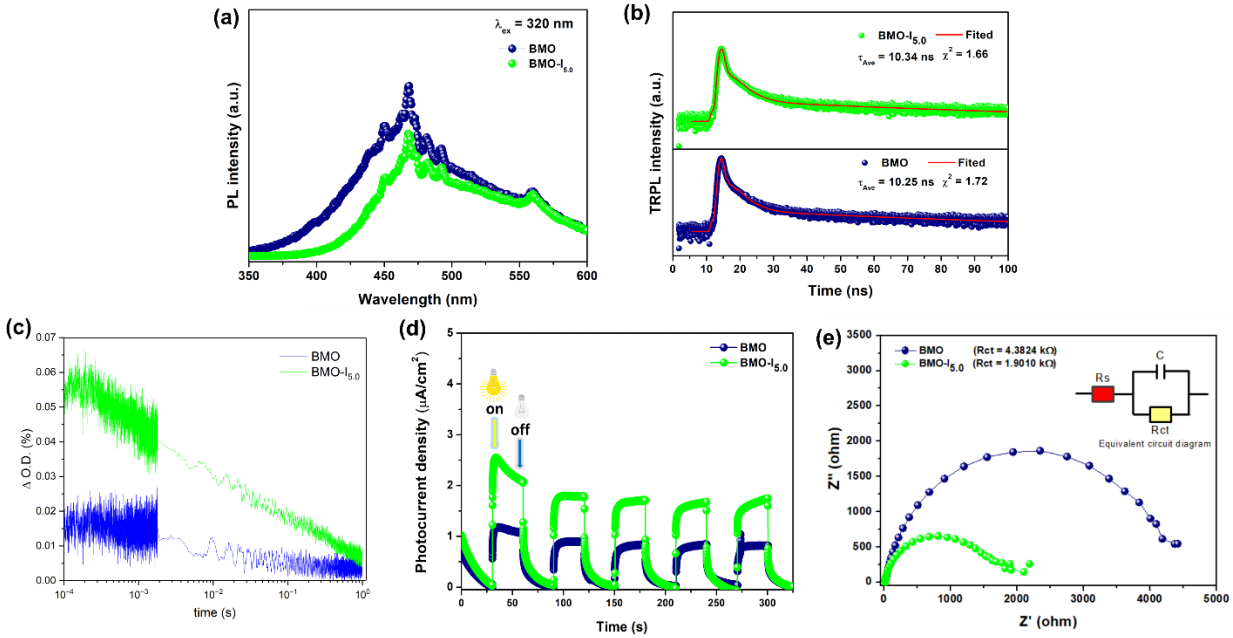

Fig.6 PL spectra (a), TRPL spectra (b), transient absorption decay kinetics (c), photocurrent response curves (d), and EIS Nyquistplots (e) of BMO and BMO-$I_{5.0}$

2.3 Computational investigation of the optoelectronic properties

To investigate carrier transport in the materials in detail, we first examined carrier behavior in Bi_2MoO_6 using computation. We modeled a supercell with an additional electron to represent a photo-excited electron. This excess electron interacts with the dielectric crystal, leading to

coupling between the electron and local lattice distortions, which results in the formation of a polaron [41]. The calculated polaron formation energy of -0.37 eV indicates that the electron is more stable as a localized polaron than as a delocalized electron in the conduction band. Local lattice distortions around the Mo center, associated with the polaron, are evident (Fig. 7a and b). Specifically, two Mo–O bond lengths (highlighted in red) increase from 1.78 Å and 1.79 Å to 1.91 Å and 1.92 Å, while the remaining bonds exhibit only slight changes. Bader charge analysis shows a reduction in the charge of the Mo center, decreasing from 2.69 to 2.49, consistent with the transition from Mo^{6+} to Mo^{5+}. The polaron localization and its electronic structure are depicted in Fig. 7c and 7d. The electron density plot reveals that the orbital contributions are primarily along the z-axis, with some extension along the x-axis, positioned between four oxygen ligands. The partial density of states (PDOS) analysis further supports the electron localization by the presence of an occupied gap state. This state is predominantly composed of the Mo $\boldsymbol{d_{z^2}}$ orbital, with minor contributions from the $\boldsymbol{d_{x^2-y^2}}$ and $\boldsymbol{d_{xz}}$ orbitals, which is consistent with the electron density plot. The negative polaron formation energy, local lattice distortions, reduction of the Mo center, and the appearance of gap states collectively support the polaron model. To the best of our knowledge, this is the first report on polaron formation in Bi_2MoO_6. These observations are consistent with previous findings suggesting the existence of polarons in other transition metal oxides, such as MoO_3[13,14], TiO_2[42], $BiVO_4$[43, 44], and Bi_2WO_6[45].

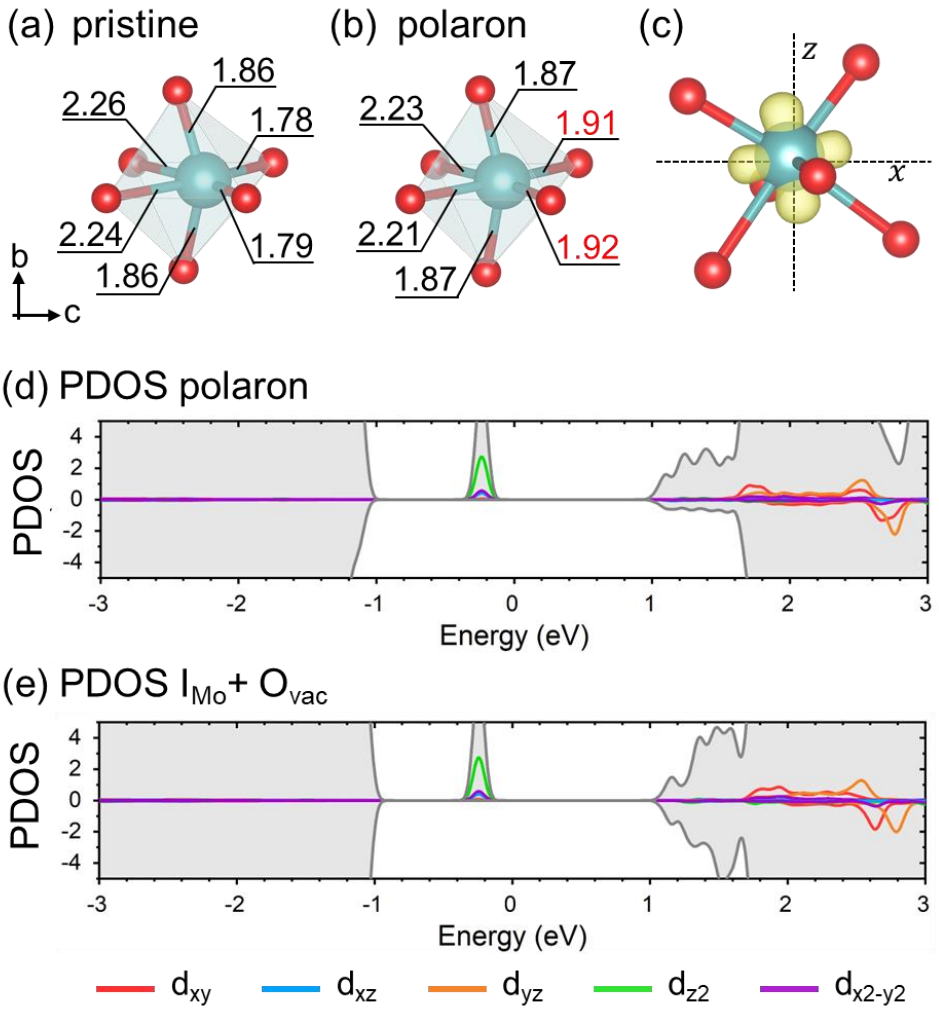

Fig. 7 (a) Local structure of Mo-center in perfect Bi_2MoO_6 and (b) the local structure distortion upon the polaron formation. The Mo-O bond lengths are shown in Å. (d) Partial density of states (PDOS) showing an occupied gap state from the polaron formation that mostly belongs to $\boldsymbol{d_{z^2}}$ orbital and (d) the corresponding electron densities as shown in yellow bulb. (c) Partial density of states (PDOS) of the I substitution for Mo coupled with oxygen vacancy (I_{MoO} + O_{vac}).

As oxygen vacancy is frequently found in this compound[46-48], we examined the oxygen vacancy formation energy in pristine and I-doped Bi_2MoO_6 and found that I substitution significantly reduces the oxygen vacancy formation energy from 2.94 eV to 1.01 eV. The lower energy barrier to form oxygen vacancies in I-doped Bi_2MoO_6 is reflected experimentally by the

higher O_V/O_L ratio observed in our the XPS results. The increased oxygen vacancies raise the intrinsic carrier density, and enhance electron transport in the material, facilitating carrier migration from the bulk to active surface sites. When the oxygen vacancy is formed near the I center ($I_{MoO} + O_{vac}$), a Mo-4d gap state appears, the Mo center charge is reduced, and lattice distortion is increased. These observations are indicative of polaron formation (Fig. 7e and Table S1). The reduced Mo charge and the lattice distortion are also supported by the experimental results. Consequently, carrier migration in both pristine and I-doped Bi_2MoO_6 follows the polaron model rather than band conduction. Given the layered crystal structure of these compounds, carrier transport is expected to be more efficient along the {100} facet compared to the {010} facet[10, 11]. This finding explains the improved charge transport observed in I-doped Bi_2MoO_6 which has a higher proportion of exposed {100} facets, highlighting the beneficial effects of I substitution in Bi_2MoO_6.

3. Conclusion

To investigate the effects of iodate (I^{5+}) substitution in Bi_2MoO_6, a series of samples were prepared by a hydrothermal method. Structural and elemental analyses confirm the successful incorporation of I^{5+} in the Bi_2MoO_6 lattice, leading to increased local lattice distortion, enhanced exposure of {100} facets, and modifications in the electronic structure. Experimental and computational results reveal that I^{5+} doping induces oxygen vacancies and increases charge carrier concentration by approximately three time. A detailed investigation confirms that charge transport in both pristine and I-doped Bi_2MoO_6 follows the small polaron model. The increased carrier concentration and greater {100} facet exposure improve charge migration in I-doped BMO. Additionally, I doping raises the Fermi energy level, positioning it above the required potential for both H_2 evolution and p-nitroaniline reduction. As a result, I-doped BMO exhibits significantly enhanced photocatalytic performance, achieving a hydrogen evolution rate of 77.53 μmol/g/h and superior p-nitroaniline reduction. This work highlights the effectiveness of iodate substitution in optimizing charge transport in layered oxides. By leveraging defect engineering and polaronic transport, this strategy provides a promising approach for designing high-performance photocatalysts for sustainable energy applications, including water splitting and selective organic transformations.

Data availability

The data supporting this article have been included as part of the ESI.† Data are also available upon request from the authors.

Conflicts of interest

There are no conflicts to declare.

Acknowledgements

This work is supported by the Research and Innovation Fund (NSRF) via the Program Management Unit for Human Resources & Institutional Development, Research and Innovation [grant number B42G670035] Suranaree University of Technology, Thailand Science Research and Innovation (TSRI) and National Science, Research and Innovation Fund (NSRF) (grant number 204263).

References

[1] M. Okazaki, Y. Wang, T. Yokoi, K. Maeda, Visible-light-driven water oxidation using anatase titania modified with first-row transition-metal-oxide nanoclusters, J. Phys. Chem. C, 123 (2019) 10429-10434, https://doi.org/10.1021/acs.jpcc.9b01222.

[2] Z. Jiang, H. Sun, T. Wang, B. Wang, W. Wei, H. Li, S. Yuan, T. An, H. Zhao, J. Yu, Nature-based catalyst for visible-light-driven photocatalytic CO_2 reduction, Energy Environ. Sci., 11 (2018) 2382-2389, https://doi.org/10.1039/C8EE01781F.

[3] L. Lin, T. Hisatomi, S. Chen, T. Takata, K. Domen, Visible-light-driven photocatalytic water splitting: recent progress and challenges, Trend. Chem., 2 (2020) 813-824, https://doi.org/10.1016/j.trechm.2020.06.006.

[4] W. Wang, X. Chen, G. Liu, Z. Shen, D. Xia, P.K. Wong, C.Y. Jimmy, Monoclinic dibismuth tetraoxide: A new visible-light-driven photocatalyst for environmental remediation, Appl. Catal. B: Environ., 176 (2015) 444-453, https://doi.org/10.1016/j.apcatb.2015.04.026.

[5] J. Yu, Y. Hai, B. Cheng, Enhanced photocatalytic H2-production activity of TiO_2 by $Ni(OH)_2$ cluster modification, J. Phys. Chem. C, 115 (2011) 4953-4958, https://doi.org/10.1021/jp111562d.

[6] S. Zhou, Y. Yang, P. Yin, Z. Ren, L. Wang, M. Wei, Metal–support synergistic catalysis in Pt/MoO_{3-x} nanorods toward ammonia borane hydrolysis with efficient hydrogen generation, ACS Appl.Mater. Interfaces, 14 (2022) 5275-5286, https://doi.org/10.1021/acsami.1c20736.

[7] J.K. Cooper, S.B. Scott, Y. Ling, J. Yang, S. Hao, Y. Li, F.M. Toma, M. Stutzmann, K. Lakshmi, I.D. Sharp, Role of hydrogen in defining the n-type character of $BiVO_4$ photoanodes, Chem. Mater., 28 (2016) 5761-5771, https://doi.org/10.1021/acs.chemmater.6b01994.

[8] J. Long, S. Wang, H. Chang, B. Zhao, B. Liu, Y. Zhou, W. Wei, X. Wang, L. Huang, W. Huang, Bi_2MoO_6 nanobelts for crystal facet-enhanced photocatalysis, Small (Weinheim an der Bergstrasse, Germany), 10 (2014) 2791-2795, 2741, https://doi.org/10.1002/smll.201302950.

[9] X. Yang, X. Li, B. Zhang, T. Liu, Z. Chen, Facet-dependent Bi_2MoO_6 for highly efficient photocatalytic selective oxidation of sp^3 C–H bonds using O_2 as an oxidant, Catal. Sci. Technol., 13 (2023) 1996-2000, https://doi.org/10.1039/D3CY00018D.

[10] S. Wang, X. Ding, N. Yang, G. Zhan, X. Zhang, G. Dong, L. Zhang, H. Chen, Insight into the effect of bromine on facet-dependent surface oxygen vacancies construction and stabilization of Bi_2MoO_6 for efficient photocatalytic NO removal, Appl. Catal. B: Environ., 265 (2020) 118585, https://doi.org/10.1016/j.apcatb.2019.118585.

[11] X. Xu, N. Yang, P. Wang, S. Wang, Y. Xiang, X. Zhang, X. Ding, H. Chen, Highly intensified molecular oxygen activation on Bi@Bi_2MoO_6 via a metallic Bi-coordinated facet-dependent effect, ACS Appl. Mater. Interfaces, 12 (2019) 1867-1876, https://doi.org/10.1021/acs.jpcc.6b01188.

[12] A. Walsh, Y. Yan, M.N. Huda, M.M. Al-Jassim, S.-H. Wei, Band edge electronic structure of $BiVO_4$: elucidating the role of the Bi s and V d orbitals, Chem. Mater., 21 (2009) 547-551, https://doi.org/10.1021/cm802894z.

[13] A. Waehayee, S. Wangngae, J. Rungruengkit, T. Lerdwiriyanupap, T. Choklap, J. Prachanat, N. Pornnongsan, A. Ruangvittayanon, H. Nakajima, T. Chankhanittha, Modulation of the Internal Electric Field in Te-Doped Bi_2MoO_6 Nanosheets: Implication for the Photocatalytic Degradation of Rhodamine B and Photooxidation of Benzylamine, ACS Appl. Nano Mater., 7 (2024) 6079-6092, https://doi.org/10.1021/acsanm.3c05941.

[14] P.S. Halasyamani, Asymmetric cation coordination in oxide materials: influence of lone-pair cations on the intra-octahedral distortion in d^0 transition metals, Chem. Mater., 16 (2004) 3586-3592, https://doi.org/10.1021/cm049297g.

[15] K.M. Ok, P.S. Halasyamani, D. Casanova, M. Llunell, P. Alemany, S. Alvarez, Distortions in octahedrally coordinated d^0 transition metal oxides: A continuous symmetry measures approach, Chem. Mater., 18 (2006) 3176-3183, https://doi.org/10.1021/cm061691m.

[16] S. Li, F. Chen, Q. An, R. Tang, H. Huang, Triggering Overall Crystal Polarization by Octahedron Elongation Distortion for Highly Boosted and Selective Aerobic Photo-Oxidation, Adv. Funct. Mater., 34 (2024) 2409035, https://doi.org/10.1002/adfm.202409035.

[17] Y. Hu, Y. Pan, Z. Wang, T. Lin, Y. Gao, B. Luo, H. Hu, F. Fan, G. Liu, L. Wang, Lattice distortion induced internal electric field in TiO_2 photoelectrode for efficient charge separation and transfer, Nature Commun., 11 (2020) 2129, https://doi.org/10.1038/s41467-020-15993-4.

[18] T. Ishihara, N.S. Baik, N. Ono, H. Nishiguchi, Y. Takita, Effects of crystal structure on photolysis of H_2O on K–Ta mixed oxide, J. Photochem. Photobiol. A: Chem., 167 (2004) 149-157, https://doi.org/10.1016/j.jphotochem.2004.03.030.

[19] X. Yang, X. Xu, J. Wang, T. Chen, S. Wang, X. Ding, H. Chen, Insights into the surface/interface modifications of Bi_2MoO_6: feasible strategies and photocatalytic applications, Solar Rrl, 5 (2021) 2000442, https://doi.org/10.1002/solr.202000442.

[20] Z. Dai, F. Qin, H. Zhao, J. Ding, Y. Liu, R. Chen, Crystal defect engineering of aurivillius Bi_2MoO_6 by Ce doping for increased reactive species production in photocatalysis, ACS Catal., 6 (2016) 3180-3192, https://doi.org/10.1021/acscatal.6b00490.

[21] Y. Chen, W. Yang, S. Gao, C. Sun, Q. Li, Synthesis of Bi_2MoO_6 nanosheets with rich oxygen vacancies by postsynthesis etching treatment for enhanced photocatalytic performance, ACS Appl. Nano Mater., 1 (2018) 3565-3578, https://doi.org/10.1021/acsanm.8b00719.

[22] G. Li, W. Yang, S. Gao, Q. Shen, J. Xue, K. Chen, Q. Li, Creation of rich oxygen vacancies in bismuth molybdate nanosheets to boost the photocatalytic nitrogen fixation performance under visible light illumination, Chem. Eng. J., 404 (2021) 127115, https://doi.org/10.1016/j.cej.2020.127115.

[23] H. Li, W. Li, F. Wang, X. Liu, C. Ren, Fabrication of two lanthanides co-doped Bi_2MoO_6 photocatalyst: selection, design and mechanism of Ln_1/Ln_2 redox couple for enhancing photocatalytic activity, *Appl. Catal. B: Environ.*, 217 (2017) 378-387, https://doi.org/10.1016/j.apcatb.2017.06.015.

[24] J. Di, X. Zhao, C. Lian, M. Ji, J. Xia, J. Xiong, W. Zhou, X. Cao, Y. She, H. Liu, Atomically-thin Bi_2MoO_6 nanosheets with vacancy pairs for improved photocatalytic CO_2 reduction, Nano Energy, 61 (2019) 54-59, https://doi.org/10.1016/j.nanoen.2019.04.029.

[25] Y. Xie, D. Liu, B. Wang, D. Li, Z. Yan, Y. Chen, J. Shen, Z. Zhang, X. Wang, Monolayer $Bi_2W_{1-x}Mo_xO_6$ Solid Solutions for Structural Polarity to Boost Photocatalytic Reduction of Nitrobenzene under Visible Light, ACS Sustainable Chem. Eng., 9 (2021) 2465-2474, https://doi.org/10.1021/acssuschemeng.0c07324.

[26] S.N. Lou, R. Amal, J. Scott, Y.H. Ng, Concentration-mediated band gap reduction of Bi_2MoO_6 photoanodes prepared by Bi^{3+} cation insertions into anodized MoO_3 thin films: structural, optical, and photoelectrochemical properties, ACS Appl. Energy Mater., 1 (2018) 3955-3964, https://doi.org/10.1021/acsaem.8b00675.

[27] R.K. Chava, N. Son, Y.S. Kim, M. Kang, Integration of perovskite type Bi_2MoO_6 nanosheets onto one dimensional CdS: a type-II heterostructured photocatalytic system for efficient charge separation in the hydrogen evolution reaction, Inorg. Chem. Front., 7 (2020) 2818-2832, https://doi.org/10.1039/D0QI00339E.

[28] S. Li, L. Bai, N. Ji, S. Yu, S. Lin, N. Tian, H. Huang, Ferroelectric polarization and thin-layered structure synergistically promoting CO_2 photoreduction of Bi_2MoO_6, J. Mater. Chem. A, 8 (2020) 9268-9277, **https://doi.org/10.1039/D0TA02102D**.

[29] R.t. Shannon, C.T. Prewitt, Effective ionic radii in oxides and fluorides, Struct. Sci., 25 (1969) 925-946, https://doi.org/10.1107/S0567740869003220.

[30] L. Zhang, T. Xu, X. Zhao, Y. Zhu, Controllable synthesis of Bi_2MoO_6 and effect of morphology and variation in local structure on photocatalytic activities, Appl. Catal. B: Environ., 98 (2010) 138-146, https://doi.org/10.1016/j.apcatb.2010.05.022.

[31] C. Murugan, A. Soundarya Mary, P. Murugan, A. Pandikumar, Enhanced Photoelectrocatalytic Water Splitting in $Bi_2Mo_{1-x}W_xO_6$ Solid Solutions: Understanding the Atomic Level Mechanism from the Experimental and First-Principles Approach, ACS Appl. Energy Mater., 6 (2023) 8410-8421, https://doi.org/10.1021/acsaem.3c01151.

[32] L. Zhang, Y. Man, Y. Zhu, Effects of Mo replacement on the structure and visible-light-induced photocatalytic performances of Bi_2WO_6 photocatalyst, ACS Catal., 1 (2011) 841-848, https://doi.org/10.1021/cs200155z.

[33] J. Wang, C. Zhao, S. Yuan, X. Li, J. Zhang, X. Hu, H. Lin, Y. Wu, Y. He, One-step fabrication of Cu-doped Bi_2MoO_6 microflower for enhancing performance in photocatalytic nitrogen fixation, J. Colloid Interf. Sci., 638 (2023) 427-438, https://doi.org/10.1016/j.jcis.2023.02.005.

[34] V. Jolivet, Y. Morizet, J. Hamon, M. Paris, T. Suzuki-Muresan, The influence of iodide on glass transition temperature of high-pressure nuclear waste glasses, J. Ame. Ceram. Soc., 104 (2021) 1360-1369, https://doi.org/10.1111/jace.17571.

[35] Q. Meng, C. Cao, J. Wang, L. Tian, Y. Huang, M. Yang, M. Wang, B. Cong, Y. Zhang, Atomically Thin Bi_2MoO_6 Nanosheets for Efficient Visible-Light Photocatalytic Nitrogen Fixation via O-Vacancy Tailored Exposure of Mo Sites, ACS Appl. Nano Mater., 7 (2024) 15808-15818, https://doi.org/10.1016/j.nanoen.2019.04.029.

[36] Y. Xu, Z. Wang, Y. Weng, Defect States and Polarons in Photocatalytic Semiconductors Revealed via Time-Resolved Spectroscopy, J. Phys. Chem. C, 128 (2024) 16275-16290, https://doi.org/10.1021/acs.jpcc.4c03688.

[37] J. Wiktor, F. Ambrosio, A. Pasquarello, Role of polarons in water splitting: the case of $BiVO_4$, ACS Energy Lett., 3 (2018) 1693-1697, https://doi.org/10.1021/acsenergylett.8b00938.

[38] Z. Ren, Z. Shi, H. Feng, Z. Xu, W. Hao, Recent progresses of polarons: fundamentals and roles in photocatalysis and photoelectrocatalysis, Adv. Sci., 11 (2024) 2305139, https://doi.org/10.1002/advs.202305139.

[39] C. Yang, Y. Zhang, F. Yue, R. Du, T. Ma, Y. Bian, R. Li, L. Guo, D. Wang, F. Fu, Co doping regulating electronic structure of Bi_2MoO_6 to construct dual active sites for photocatalytic nitrogen fixation, Appl. Catal.s B: Environ., 338 (2023) 123057, https://doi.org/10.1016/j.apcatb.2023.123057.

[40] B. Moss, K.K. Lim, A. Beltram, S. Moniz, J. Tang, P. Fornasiero, P. Barnes, J. Durrant, A. Kafizas, Comparing photoelectrochemical water oxidation, recombination kinetics and charge trapping in the three polymorphs of TiO_2, Sci. Rep., 7 (2017) 2938, https://doi.org/10.1038/s41598-017-03065-5.

[41] F. Cesare, R. Michele, S. Martin, D. Ulrike, Polarons in materials, Nat. Rev. Mater., 6 (2021) 560-586, https://doi.org/10.1038/s41578-021-00289-w.

[42] C. Di Valentin, A. Selloni, Bulk and surface polarons in photoexcited anatase TiO_2, J. Phys. Chem. Lett., 2 (2011) 2223-2228, https://doi.org/10.1021/jz2009874.

[43] H. Wu, L. Zhang, S. Qu, A. Du, J. Tang, Y.H. Ng, Polaron-mediated transport in $BiVO_4$ photoanodes for solar water oxidation, ACS Energy Lett., 8 (2023) 2177-2184, https://doi.org/10.1021/acsenergylett.3c00465.

[44] A.J. Rettie, H.C. Lee, L.G. Marshall, J.-F. Lin, C. Capan, J. Lindemuth, J.S. McCloy, J. Zhou, A.J. Bard, C.B. Mullins, Combined charge carrier transport and photoelectrochemical characterization of $BiVO_4$ single crystals: intrinsic behavior of a complex metal oxide, J. Ame. Chem. Soc., 135 (2013) 11389-11396, https://doi.org/10.1021/ja405550k.

[45] B. Moss, H. Le, S. Corby, K. Morita, S. Selim, C. Sotelo-Vazquez, Y. Chen, A. Borthwick, A. Wilson, C. Blackman, Anisotropic electron transport limits performance of Bi_2WO_6 photoanodes, J. Phys. Chem. C, 124 (2020) 18859-18867, https://doi.org/10.1021/acs.jpcc.0c03539.

[46] M. Sharma, A. Kumar, D. Gill, S. Jaiswal, A. Patra, S. Bhattacharya, V. Krishnan, Boosting photocatalytic nitrogen fixation via nanoarchitectonics using oxygen vacancy regulation in W-doped Bi_2MoO_6 nanosheets, ACS Appl. Mater. Interfaces, 15 (2023) 55765-55778, https://doi.org/10.1021/acsami.3c12563.

[47] Y. Wang, J. Wang, Q. Zhu, K. Zhao, H. Ren, H. Kang, M. Luo, C. Wang, Spherical Bi2MoO6 with oxygen vacancies via solvent manipulation for enhanced photocatalytic NO removal, J. Environ. Chem. Eng., 13 (2025) 115046, https://doi.org/10.1016/j.jece.2024.115046.

[48] X. Yang, X. Li, B. Zhang, T. Liu, Z. Chen, Oxygen vacancies enriched hollow Bi_2MoO_6 microspheres for efficient photocatalytic oxidation of hydrocarbons, ACS Sustainable Chem. Eng., 12 (2024) 6519-6528, https://doi.org/10.1021/acssuschemeng.3c07871.